



Positively charged nickel-sulfur dual sites for efficient CO₂ electroreduction reaction

Xiaohui Sun^{a,*}, Linglong Wang^a, Xingying Lan^a, Qing Lu^c, Yongxiao Tuo^{c,*}, Chenliang Ye^d, Dingsheng Wang^{b,*}, Chunming Xu^a

^a College of Carbon Neutrality Future Technology, China University of Petroleum (Beijing), Beijing 102249, PR China

^b Department of Chemistry, Tsinghua University, Beijing 100084, PR China

^c Department of Materials Science and Engineering, China University of Petroleum (East China), Qingdao 266580, PR China

^d College of Materials Science and Engineering, Shenzhen University, Shenzhen 518060, PR China

ARTICLE INFO

Keywords:

Single Ni atom
Electron localization
Sulfur
Dual sites
CO₂ electroreduction

ABSTRACT

Electrochemical CO₂ reduction (CO₂RR) into chemicals and fuels has gained great interest, but is subjected to low current density and poor product selectivity. Here a theory-guided design of sulfur-doped single nickel atom catalyst (Ni-SAC/SNC) with the optimal Ni-S dual active configuration was present for efficient CO₂RR. Experiments combined with theory verified that the positively charged Ni-S dual sites drastically promoted the electronic localization of Ni center, which improved the stabilization of key COOH* intermediate and thus boosted CO production on Ni. This catalyst exhibited a high CO Faradaic efficiency of ~98% and a current density of ~32.5 mA cm⁻² at a low overpotential of 620 mV, which exceeded most of single-atom electrocatalysts. This work offers atomic-level insights into the correlation between the electronic density of atomic sites and CO₂RR performance, promoting the theory-guided rational design of efficient catalysts.

1. Introduction

Electrochemical CO₂ reduction (CO₂RR) powered by renewable electricity is a promising approach to produce value-added chemicals and fuels [1–4]. Among these products, CO is an important feedstock for the chemical industry and it is of particular interest from the perspective of the market scale and economic viability [5–7]. Because of its chemical inertness, a high overpotential is normally necessary to activate CO₂. However, at a high overpotential, hydrogen evolution reaction (HER) is normally dominated and extremely reduces the energetic efficiency as well as CO selectivity [8–11]. Thus, the development of efficient catalysts capable of catalyzing CO₂RR to CO at low overpotentials is desirable but remains challenging.

Various polycrystalline metal electrocatalysts have been extensively investigated for CO₂RR to CO, such as Au, Ag and their alloys [12–18]. Considering the limited supply of noble metals, catalysts comprised of base metals are more attractive for practical application [19–22]. Yet, these nanostructured metals (i.e. Fe Co Ni etc.) are more active in HER for H₂ production [23–25]. Recently, nitrogen-doped carbon supported single atom catalysts (SACs) (denoted as M-N_x) have shown enormous

potential for CO₂RR to CO [26–29]. However, the inferior local electron density of metal center hinders first electron transfer for the stabilization of *COOH, resulting in a poor CO production rate [30–33]. Hence, optimizing the electronic structure of single metal sites would be a reasonable strategy to boost their intrinsic CO₂RR activity.

Numerous factors are known to adjust the electronic states of atomically dispersed sites, including coordination structure and number, vacancy, and local strain [34–39]. Research on the coordination environment of single atom center has gained great interests [40–42]. For instance, reducing the coordination numbers of Ni from a Ni-N₄ configuration to Ni-N₃ was found to increase the electron density of metal center, and facilitate the generation of *COOH in CO₂RR [36,39]. Alternatively, heteroatoms (such as S, P, and halogens etc.) can also tailor the electron properties of SACs [43–45]. Wang et al. reported that P in the third coordination shell of Fe enhanced the electron localization of Fe-N₄O, and thus stabilized *COOH on Fe [46]. Jiang et al. claimed that the axially coordinated Cl atom remarkably facilitated the formation of *COOH on Ni-N₄ by delocalizing the electronic states of Ni [47]. Obviously, heteroatom induced optimal electronic properties of single metal sites for CO₂RR differ from the electronegativity and coordination

* Corresponding authors.

E-mail addresses: sunxiaohui@cup.edu.cn (X. Sun), yxtuo@upc.edu.cn (Y. Tuo), wangdingsheng@mail.tsinghua.edu.cn (D. Wang).

<https://doi.org/10.1016/j.apcatb.2023.123389>

Received 22 August 2023; Received in revised form 28 September 2023; Accepted 8 October 2023

Available online 10 October 2023

0926-3373/© 2023 Elsevier B.V. All rights reserved.

shell of dopants. Thus, in-depth comprehension of how the local coordination relationship between single metal center and dopant affects the electronic properties of single metal sites could guide rational design of highly active CO₂RR catalysts.

S is a p-block element with a lower electronegativity than N. It could be used to modify the electronic structures of metal sites, which is supposed to significantly improve the catalytic performance of single-atom catalysts. Herein, we chose a moderately electronegative sulfur atom to present a theory-guided design of sulfur-doped single Ni atom catalyst for CO₂RR. Density functional theory (DFT) calculations manifested that incorporating single S atom, especially in the first coordination sphere of Ni in the form of Ni-S bonding in the carbon matrix facilitated the electronic localization of Ni center, which stabilized the key COOH* intermediate and thus boosted CO production on Ni. Guided by DFT analysis, we fabricated a single Ni atom catalyst through a modular approach with an optimal Ni-S dual active moiety supported on hollow nitrogen doped carbon sphere (Ni-SAC/SNC). Advanced characterization studies highlighted that the Ni-S bonding directly lowered the oxidation state of Ni in Ni-N₃S₁ than of Ni in Ni-N₄, in consistence with theory. The as-synthesized Ni-SAC/SNC displayed a CO Faradaic efficiency (FE_{CO}) of 98% and a stable CO partial current density (j_{CO}) of $\sim 30 \text{ mA cm}^{-2}$ for at least 24 h at a low overpotential of 620 mV, surpassing most of the reported single-atom catalysts.

2. Experimental

2.1. Materials

1-allyl-2-thiourea (purity 99%), nickel chloride hexahydrate (NiCl₂·6 H₂O, >98%), tetraethyl orthosilicate (TEOS $\geq 98\%$), and dopamine hydrochloride (99%) were purchased from Alfa. Ammonium hydroxide (NH₃·H₂O, 25 wt%), ethanol (>99.5%), and hydrofluoric acid (HF) were purchased from Acros. All the chemicals were used without further purification.

2.2. Catalyst synthesis

For the synthesis of the silica nanosphere, silica nanospheres were synthesized by using the Stober method with some modification [48]. Typically, 5 ml of TEOS was added into 175 ml of ethanol, and 6 ml of NH₃·H₂O was added into 35 ml of H₂O under stirring. Then the NH₃·H₂O solution was dropped into the TEOS solution, and the mixture was vigorously stirred for 24 h. Finally, SiO₂ nanospheres were separated by centrifugation, washed with H₂O and ethanol, and dried at 80 °C.

For the synthesis of single Ni atom on sulfur and nitrogen co-doped carbon (Ni-SAC/SNC), 1 g SiO₂ nanospheres were dispersed in 4 ml H₂O. At the same time, 1 g 1-allyl-2-thiourea and 2 mg NiCl₂·6H₂O were dissolved in 1 ml H₂O at 80 °C. The Ni-containing solution was added into the SiO₂ suspension, and stirred at 80 °C for 4 h. Afterwards, the mixture was transferred into an oven at 60 °C to remove H₂O. The residual white powder was then pyrolyzed at 900 °C for 3 h under nitrogen with a ramping rate of 5 °C/min. The Ni-SAC/SNC sample was finally obtained by leaching the SiO₂ sphere with 15 wt% HF, followed by drying at 60 °C under vacuum. Sulfur and nitrogen co-doped carbon (SNC) was prepared with a similar approach as that of Ni-SAC/SNC except no NiCl₂·6H₂O was included.

For the synthesis of single Ni atom on nitrogen doped carbon (Ni-SAC/NC), 100 mg SiO₂ nanospheres were dispersed in 200 ml H₂O. At the same time, 100 mg dopamine hydrochloride and 3 mg NiCl₂·6H₂O were first dissolved in 20 ml H₂O, and further added into the SiO₂ suspension under stirring. Then, a tris (hydroxymethyl)aminomethane solution (200 mg in 10 ml H₂O) was dropped into the above solution to tune the pH value to 8.5. The mixture was stirred for another 20 h, and the black powder was separated by filtration, dried under vacuum at 80 °C and further pyrolyzed at 900 °C under nitrogen. Finally, Ni-SAC/NC was obtained by leaching the SiO₂ sphere with 15 wt% HF and

drying at 60 °C under vacuum. Nitrogen doped carbon (NC) was prepared with a similar approach as that of Ni-SAC/NC except no NiCl₂·6H₂O was included.

2.3. Characterization

Transmission electron microscopy (TEM) and high-resolution TEM (HR-TEM) were carried out by a Hitachi HT7700 working at 100 kV and a FEI Tecnai G2 F20 S-Twin working at 200 kV. The atomic structure of Ni-SAC/SNC was characterized with an ARM-200CF (JEOL, Tokyo, Japan) transmission electron microscope operated at 200 keV and equipped with double spherical aberration (Cs) correctors. The Ni content of Ni-SAC/SNC was measured by ICP-OES (iCAP6300). X-ray diffraction (XRD) patterns were analyzed by a Rigaku RU-200b X-ray diffractometer equipped with a Cu-K α radiation ($\lambda = 0.15406 \text{ nm}$). The Brunauer-Emmett-Teller (BET) surface areas of the as-synthesized catalysts were characterized by a Micromeritics ASAP 2020 nitrogen adsorption apparatus at 77 K. Raman spectra of the samples were analyzed on the LabRAM HR Evolution. XPS spectra were performed by a Thermo Fisher ESCALAB Scientific ESCALAB 250Xi XPS System. The X-ray absorption fine structure (XAFS) spectra were performed at beamline 11B of the SiP-ME2 platform of the Shanghai Synchrotron Radiation Facility (SSRF). The XAFS data of Ni-SAC/SNC and Ni-SAC/NC were recorded in the fluorescence excitation mode with a Lytle detector at room temperature. Ni foil, NiO and NiPc were used as references and measured in a transmission mode using ionization chamber.

2.4. Electrochemical measurements for CO₂RR

Electrochemical measurements for CO₂RR were carried out in an H-type electrolytic cell, and the compartments were separated by a proton exchange membrane (Nafion® N117, Dupont), and filled with 30 ml of a 0.5 M KHCO₃ solution. Platinum net electrode, Ag/AgCl, and carbon fiber paper were used as the counter electrode, the reference electrode, and the working electrode, respectively.

For the preparation of catalyst ink, 5 mg of the catalyst and 20 μL Nafion solution (5 wt%) were dispersed in 500 μL ethanol by a sonication treatment. Afterwards, 50 μL of the slurry was homogeneously painted onto a carbon fiber paper electrode ($0.5 \times 0.5 \text{ cm}^2$) with a loading of $\sim 2 \text{ mg cm}^{-2}$. All the electrochemical tests were performed at room temperature. Prior to the CO₂RR test, a high-purity CO₂ gas was flowed into the electrolyte solution (0.5 M KHCO₃) for at least 30 min during the measurement, the tested potentials ($E_{\text{Ag/AgCl}}$) were calibrated to the reversible hydrogen electrode (E_{RHE}) potentials based on the equation: $E_{\text{RHE}} = E_{\text{Ag/AgCl}} + 0.0591 \times \text{pH} + 0.197$. The LSV curves were analyzed on the Gamry Reference 600 electrochemical workstation at a 10 mV s⁻¹ scan rate. The electrochemical impedance spectroscopy (EIS) experiments were performed by applying an AC voltage with 10 mV amplitude with a frequency ranging from 10⁵ to 0.1 Hz at -1.385 V vs. RHE . The electrochemical double-layer capacitance (C_{dl}) was calculated by the CV method at different scan rates between 5 and 35 mV s⁻¹ within a non-faradic potential range from 1.00 to 1.10 V vs. RHE. The gaseous products were analyzed by an online GC. H₂ was detected by a thermal conductivity detector (TCD) for and CO was detected by a flame ionization detector (FID).

The Faradaic efficiency of gas products was calculated by the equation as follows:

$$FE_{\text{gas product}} = \frac{N \times F \left(\frac{\text{C}}{\text{mol}} \right) \times V \left(\frac{\text{mL}}{\text{min}} \right) \times 10^{-6} \left(\frac{\text{m}^3}{\text{mol}} \right) \times v(\text{vol}\%) \times 1.013 \times 10^5 \left(\frac{\text{N}}{\text{m}^2} \right)}{8.314 \left(\text{N} \cdot \frac{\text{m}}{\text{mol} \cdot \text{K}} \right) \times 298.15 \text{ K} \times I_{\text{total}} \left(\frac{\text{C}}{\text{s}} \right) \times 60 \left(\frac{\text{s}}{\text{min}} \right)}$$

FE (%) = faradaic efficiency for CO or H₂;

N = electron transfer number, which is 2 for CO;

F (C/mol) = Faradaic constant, 96485 C/mol;

V (mL/min) = gas flow rate measured by a flowmeter at the outlet of the cell under ambient conditions;

v (vol %) = volume concentration of gaseous products (CO or H₂) from GC;

I_{total} (C/s) = cell current at steady state obtained by electrochemical workstation.

The Tafel slope for CO₂RR was calculated by the following formula:

$$\eta = b \log \left(\frac{j}{j_0} \right)$$

η (mV) = Overpotential;

b (mV/dec) = Tafel slope;

j (mA/cm²) = Current density;

j_0 (mA/cm²) = Exchange current density.

The turnover frequency (TOF) for CO formation was calculated using the following equation:

$$TOF = \frac{j_{CO} \times S / (N \times F)}{m_{cat} \times \omega / M} \times 3600$$

j_{CO} (A/cm²) = partial current density for CO production;

S (cm²) = geometric surface area of working electrode;

N = electron transfer number, which is 2 for CO₂;

F (C/mol) = Faradaic constant, 96485;

m_{cat} (g) = mass of catalyst on the electrode;

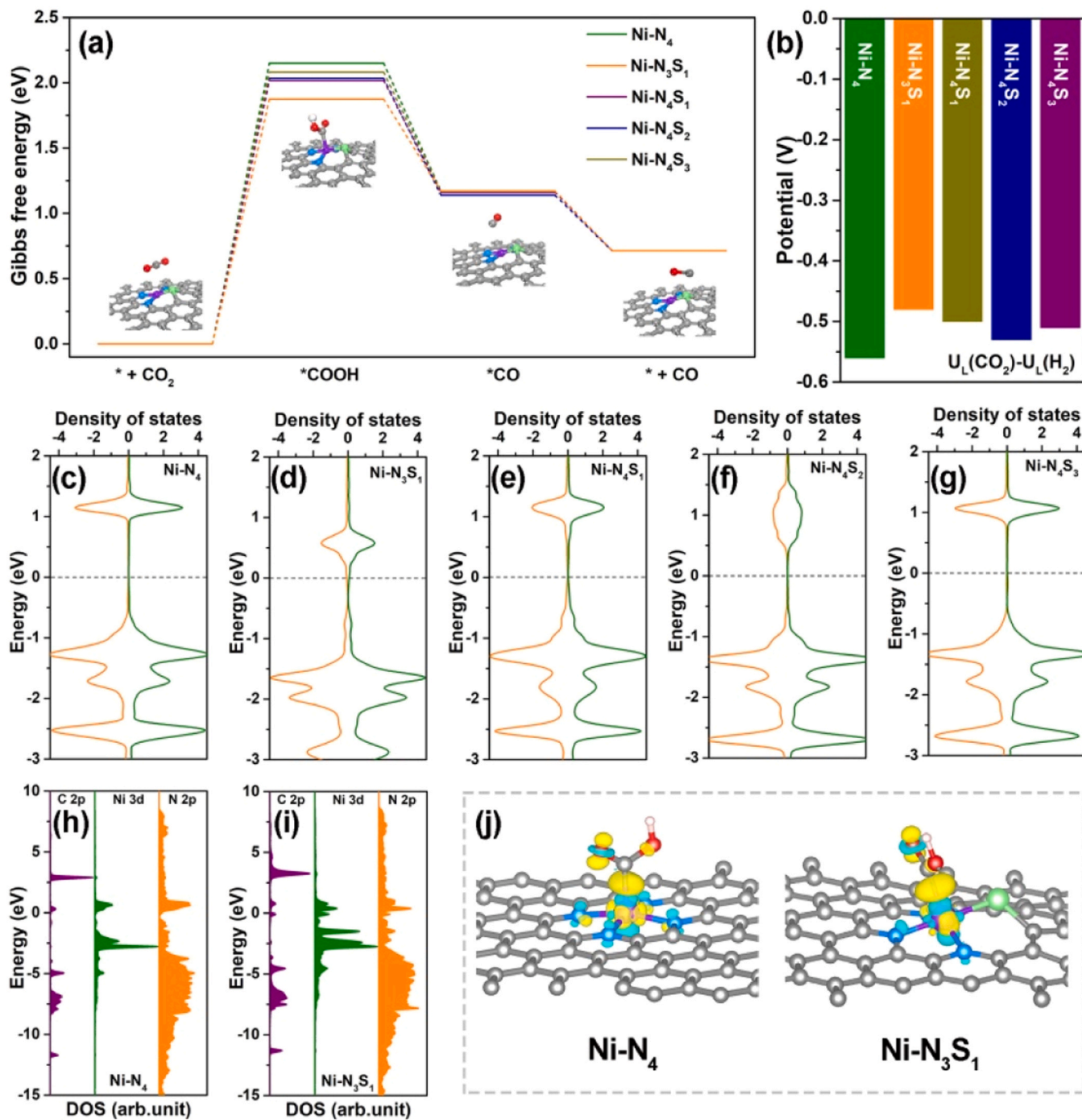


Fig. 1. (a) Calculated free energy diagrams for CO₂RR to CO and (b) variation of the difference between the limiting potentials of CO₂RR and HER over different models; (c-g) Density of states (DOS) of Ni-N₄, Ni-N₃S₁, Ni-N₄S₁, Ni-N₄S₂ and Ni-N₄S₃ (olive: Ni spin up; orange: Ni spin down); (h, i) DOS of the orbital interaction between N 2p, Ni 3d and C 2p of COOH* for Ni-N₄ and Ni-N₃S₁; (j) Differential charge density of Ni-N₄ and Ni-N₃S₁ (yellow: accumulation; cyan: depletion; isosurface value = 0.006 eÅ⁻³).

ω (%) = content of single-atom metal in the catalyst;

M (g/mol) = atomic mass of single-atom metal.

2.5. Computational details

DFT calculations were performed using the Vienna ab initio simulation package (VASP) with the Perdew-Burke-Ernzerhof (PBE) functional, which accounts for the exchange-correlation energy based on the generalized gradient approximation. The projected augmented wave (PAW) method, along with a plane-wave basis set, was employed to describe the valence-core interactions [49]. The plane wave cut-off energy was optimized to 450 eV, and the Brillouin zone was sampled using a $5 \times 5 \times 1$ k-point mesh. For each atom, the ionic relaxation force criterion was set to 0.03 eV/Å, and the threshold of energy convergence for each iteration was 10^{-5} eV.

The NiN₄ model was constructed by bonding a Ni atom to four pyridinic-N atoms on a $6 \times 6 \times 1$ graphene monolayer. In the case of the Ni-N₃S₁ model, one of the N atoms in Ni-N₄ model was replaced with a S atom. For the Ni-N₄S₁, Ni-N₄S₂ and Ni-N₄S₃ models, one of the C atoms in different shell coordination around the Ni-N₄ center in the Ni-N₄ model was substituted with a S atom. The geometries of Ni-N₄, Ni-N₃S₁, Ni-N₄S₁, Ni-N₄S₂ and Ni-N₄S₃ were simulated based on the principle of optimal energy, and the optimized geometries are demonstrated in Fig. S1.

The Gibbs free energy barrier of the reaction pathway was calculated as $\Delta G = \Delta E_{\text{ads}} + \Delta E_{\text{ZPE}} - T\Delta S_{\text{ads}}$, where ΔE_{ads} represents the electronic adsorption energy, ΔE_{ZPE} represents the zero-point energy difference between the adsorbed and gaseous species, and $T\Delta S_{\text{ads}}$ represents the corresponding entropy difference between these two states (T was set to be 298 K).

3. Results and discussion

3.1. Theory-guided design of the sulfur-doped single Ni atom catalyst for CO₂RR

To study the relationship between local coordination structure induced electronic properties and the reaction energetics of CO₂RR and HER, we built a graphene layer with a Ni-N₄ configuration, and optimized single S atom in different coordination shell of Ni center with the lowest formation energy among the different locations, namely, Ni-N₃S₁ (S in the first shell of Ni), Ni-N₄S₁ (S in the second shell of Ni), Ni-N₄S₂ (S in the third shell of Ni) and Ni-N₄S₃ (S in the fourth shell of Ni) (Fig. S1). The Gibbs reaction energy profiles of CO₂RR for different models are present in Fig. 1a. Apparently, the presence of S lowered the reaction Gibbs free energy (ΔG) of first electron transferring step ($\text{CO}_2^* + \text{H}^+ + \text{e}^- \rightarrow \text{*COOH}$) compared to Ni-N₄, and this value largely depended on the position of S. When S was incorporated in the first shell and directly bonded with Ni in the form of Ni-N₃S₁, the ΔG displayed a value of 1.87 eV, much lower than that of Ni-N₄S₁ (2.02 eV), Ni-N₄S₂ (2.07 eV), Ni-N₄S₃ (2.09 eV) and Ni-N₄ (2.15 eV), representing the highest activity for *COOH formation among these configurations. Owing to the exothermic feature of the second electron transfer step ($\text{COOH}^* + \text{H}^+ + \text{e}^- \rightarrow \text{CO}^*$) for these models, the first electron transfer step is the rate determining step (RDS). Interestingly, although the existence of S also promoted the HER activity of single Ni site, the deviation in limiting potentials (U_L) of CO₂RR and HER ($\Delta U_L = U_L(\text{CO}_2) - U_L(\text{H}_2)$) revealed a less negative value in the S containing models, especially for Ni-N₃S₁ than Ni-N₄ (Fig. 1b and S2). Such a less negative value for Ni-N₃S₁ refers to a higher selectivity toward CO compared to the other counterpart [50].

We further analyzed the electronic property of Ni center in these models. Incorporating S in the system was found to modify the charge density distributions. As shown in Fig. 1c-g, the electronic density around the Fermi level of Ni-N₃S₁ had a more remarkable contribution from Ni than that of Ni-N₄S₁, Ni-N₄S₂, Ni-N₄S₃ and Ni-N₄. Such

electronic alteration was also reflected by Bader charge analysis, and Ni in Ni-N₃S₁ (+0.72e) exhibited a much lower oxidation state than that in Ni-N₄S₁ (+0.83e), Ni-N₄S₂ (+0.84e), Ni-N₄S₃ (+0.86e) and Ni-N₄ (+0.87e). Apparently, when positively charged S was directly bonded with Ni in Ni-N₃S₁, the electron-deficient state around Ni is significantly attenuated (Fig. S3). Indeed, owing to the lower oxidation state of Ni, more electrons could be donated from the Ni center in Ni-N₃S₁ to stabilize *COOH with much less assistance from adjacent N atoms by means of weak hybridization in the case of Ni-N₄ (Fig. 1j), which substantially reduced the energy barrier for *COOH formation. This is also evidenced by the partial DOS analysis, and a more pronounced overlap between Ni 3d and C 2p of COOH* was detected in Ni-N₃S₁ than in Ni-N₄ (Fig. 1h-i). Therefore, the electron enriched Ni center induced by Ni-S coordination endows Ni-N₃S₁ highly active for CO₂RR to CO compared to the rest counterparts.

3.2. Preparation and characterization of the Ni-SAC/SNC catalyst

In light of the outstanding CO₂RR performance of Ni-N₃S₁ model derived from DFT calculations, we introduced a modular approach to fabricate a unique single-atom Ni catalyst with an optimal Ni-S dual active configuration supported on hollow nitrogen doped carbon sphere. As shown in Fig. 2a, a nickel complex was first synthesized by coordinating Ni cations with N and S atoms in 1-allyl-2-thiourea, and further coated on SiO₂ nanospheres with a diameter of ~150 nm (Fig. S4). The core-shell SiO₂@nickel complex was pyrolyzed in N₂ and subsequently leached in hydrofluoric acid to generate Ni-SAC/SNC. Transmission electron microscopy (TEM) analysis verified that Ni-SAC/SNC and Ni-SAC/NC displayed a hollow spherical structure with no Ni nanoparticles (NPs) present (Fig. 2b and Fig. S5a). High-angle annular dark-field scanning TEM (HAADF-STEM) demonstrated some bright dots to homogeneously distribute in Ni-SAC/SNC, confirming the existence of atomically dispersed Ni (Fig. 2c). The energy-dispersive X-ray spectroscopy (EDX) analysis revealed a uniform distribution of C, N, S and Ni signals in Ni-SAC/SNC (Fig. S5b and Fig. 2d-g), and a Ni loading of ~0.3 wt% was determined with the inductively coupled plasma optical emission spectrometry (ICP-OES) analysis.

Powder X-ray diffraction (XRD) analysis exhibited only two diffractions at $2\theta = 30^\circ$ and 50.5° in Ni-SAC/SNC and Ni-SAC/NC, assigned to the (0 0 2) and (1 0 0) planes of the graphitic carbon, respectively (Fig. S6) [51]. Raman spectra of Ni-SAC/SNC and Ni-SAC/NC displayed a similar intensity ratio between D band (1350 cm^{-1}) and G band (1580 cm^{-1}), suggestive of a comparable degree of graphitization (Fig. S7) [52]. N₂ adsorption tests clearly revealed a similar surface area between Ni-SAC/SNC and Ni-SAC/NC, and the presence of hysteresis loop at P/P₀ of 0.4 manifested the mesoporous structure inside the nanoparticles (Fig. S8 and Table S1) [53].

The surface composition and elemental states of these catalysts were studied by X-ray photoelectron spectroscopy (XPS). XPS survey clearly demonstrated the presence of C, N, O, and Ni in both Ni-SAC/SNC and Ni-SAC/NC with the N loadings of 6.4 at% and 5.1 at% in Ni-SAC/SNC and Ni-SAC/NC, respectively. Moreover, S was also detected in Ni-SAC/SNC with a content of 1.2 at%. The Ni *s* spectra of Ni-SAC/SNC and Ni-SAC/NC were deconvoluted into five types of nitrogen species, namely, pyridinic-N (398.5 eV), Ni-N coordination (399.1 eV), pyrrolic-N (399.9 eV), quaternary-N (400.9 eV), and oxidized-N (402.4 eV) (Fig. 3a and Fig. S9) [54–57]. For Ni-SAC/SNC and SNC, the S2p signals clearly manifested the presence of C-S-C (~164.0 eV), C=S-C (~165.0 eV) and sulfate (C-SO_x) (~168.3 eV) (Fig. 3b and S10) [58,59]. Besides, an extra peak at ~163.0 eV was detected in Ni-SAC/SNC, attributed to the Ni-S coordination [60]. For the Ni2p signals, the binding energy for Ni-SAC/SNC (~854.4 eV) was slightly lower than that of Ni-SAC/NC (~854.7 eV), indicative of a lower valent state of Ni in Ni-SAC/SNC (Fig. S11). Clearly, this peak is located between those of Ni⁰ (~853.5 eV) and NiO (~855.8 eV), suggesting an electro-positive Ni^{δ+} (0 < δ < 2). Such low valent-state Ni with partially occupied 3d

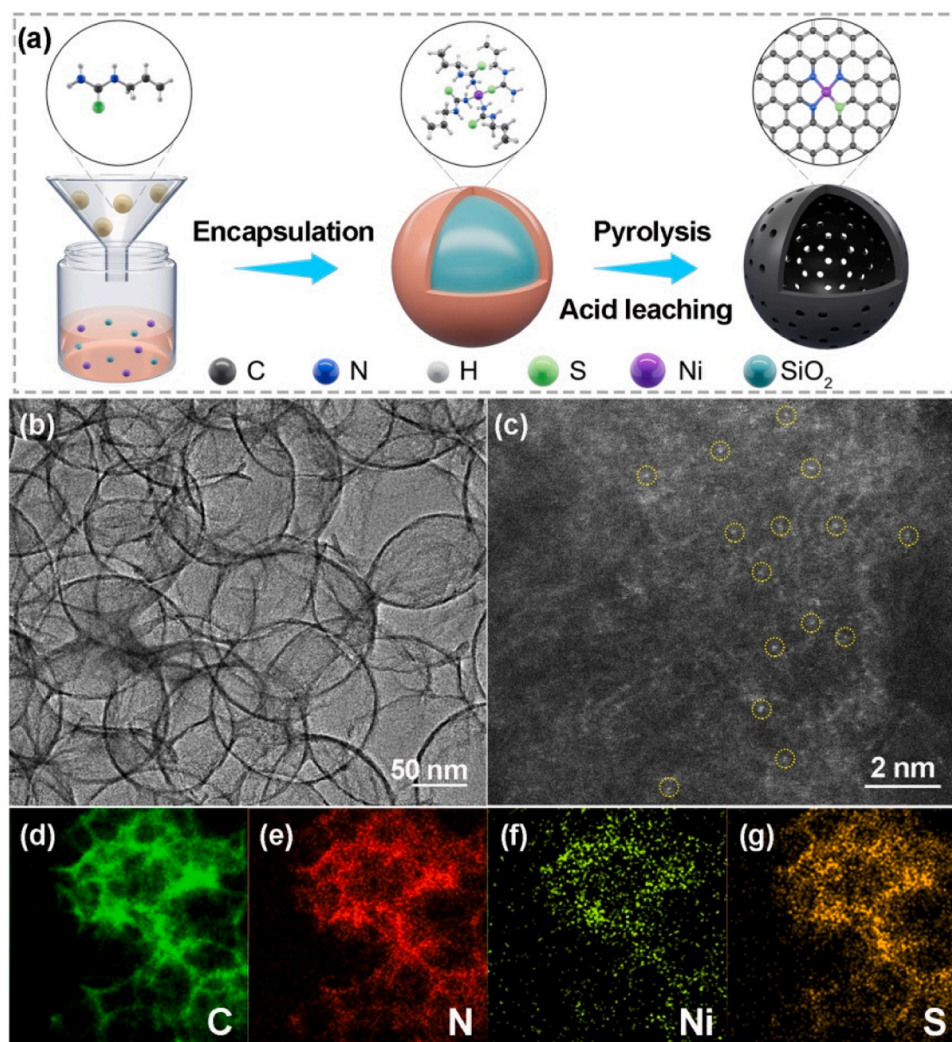


Fig. 2. Synthesis and morphological characterizations of Ni-SAC/SNC. (a) Scheme of the synthesis of Ni-SAC/SNC. (b) TEM image, (c) HAADF-STEM image, and (d-g) EDS maps of Ni-SAC/SNC.

orbital was supposed to be highly active for the activation of small molecules.

Ni *K*-edge X-ray absorption spectroscopy (XAS) measurements were carried out to explore the electronic and geometric structure of Ni in Ni-SAC/SNC and Ni-SAC/NC. The white line intensity of two catalysts in X-ray absorption near edge structure (XANES) spectra was situated between those of Ni⁰ and NiO, suggesting the partially oxidized state of Ni in both samples (Fig. 3c) [61]. Ni-SAC/SNC showed a lower intensity than Ni-SAC/NC, indicating that the presence of S in the carbon matrix reduced the oxidation state of Ni, in line with the XPS result. To probe the local structural information of Ni-SAC/SNC and Ni-SAC/NC, Fourier transformations extended X-ray absorption fine structure (FT-EXAFS) analysis was conducted. Both samples exhibited the main peak at ~ 1.42 Å, primarily ascribed to the scattering of Ni-N coordination, and the absence of Ni-Ni scattering at ~ 2.17 Å demonstrated the atomically dispersed Ni in both catalysts (Fig. 3d). For Ni-SAC/SNC, a small peak at ~ 1.90 Å was also detected, which was derived from the Ni-S scattering interaction. By fitting the FT-EXAFS spectra of both catalysts in *R* space, the local configuration of Ni was determined. The Ni atom was coordinated by three N atoms and one S atom in Ni-SAC/SNC, while Ni was surrounded by four N atoms in Ni-SAC/NC (Fig. S12, S13, and Table S2).

3.3. Catalytic performance of the Ni-SAC/SNC catalyst for CO₂RR

Inspired by the unique structural features of Ni-SAC/SNC, the CO₂ electrocatalytic performance was further evaluated by linear sweep voltammetry (LSV) in a three-electrode system with CO₂-saturated 0.5 M KHCO₃ electrolyte (Fig. S14). Apparently, the $j(\text{N}_2)$ in the N₂-saturated KHCO₃ solution was attributed to HER. After introducing CO₂ in the electrolyte, the $j(\text{CO}_2)$ was much higher than $j(\text{N}_2)$. This suggested that both CO₂RR and HER contributed to $j(\text{CO}_2)$ in the CO₂-saturated solutions. Only CO and H₂ were detected during CO₂RR (Fig. 4a and S15). Ni-SAC/SNC showed a FE_{CO} above 90% in a wide potential range from -0.53 to -1.03 V vs. RHE, much higher than that of Ni-SAC/NC. At the same time, Ni-SAC/SNC also exhibited a lower FE_{H_2} in the overall potential range than Ni-SAC/NC, highlighting that the incorporation of S significantly boosted CO₂RR by suppressing the HER activity. Specifically, the FE_{CO} reached $\sim 98\%$ with a j_{CO} of ~ 32.5 mA cm⁻² at an overpotential of 620 mV, which surpassed most of the reported SACs (Fig. 4b and Table S3). Moreover, the turnover frequency (TOF) per nickel site for CO production at -0.73 V vs. RHE was calculated as 5860 h⁻¹, which is among the highly active SACs for CO₂RR, highlighting the eminent activity of Ni in Ni-SAC/SNC (Table S3). The long-term CO₂RR test for Ni-SAC/SNC was also performed at an overpotential of ~ 620 mV, and no apparent deactivation was observed after 24 h testing, manifesting the outstanding cycling stability (Fig. 4c). After

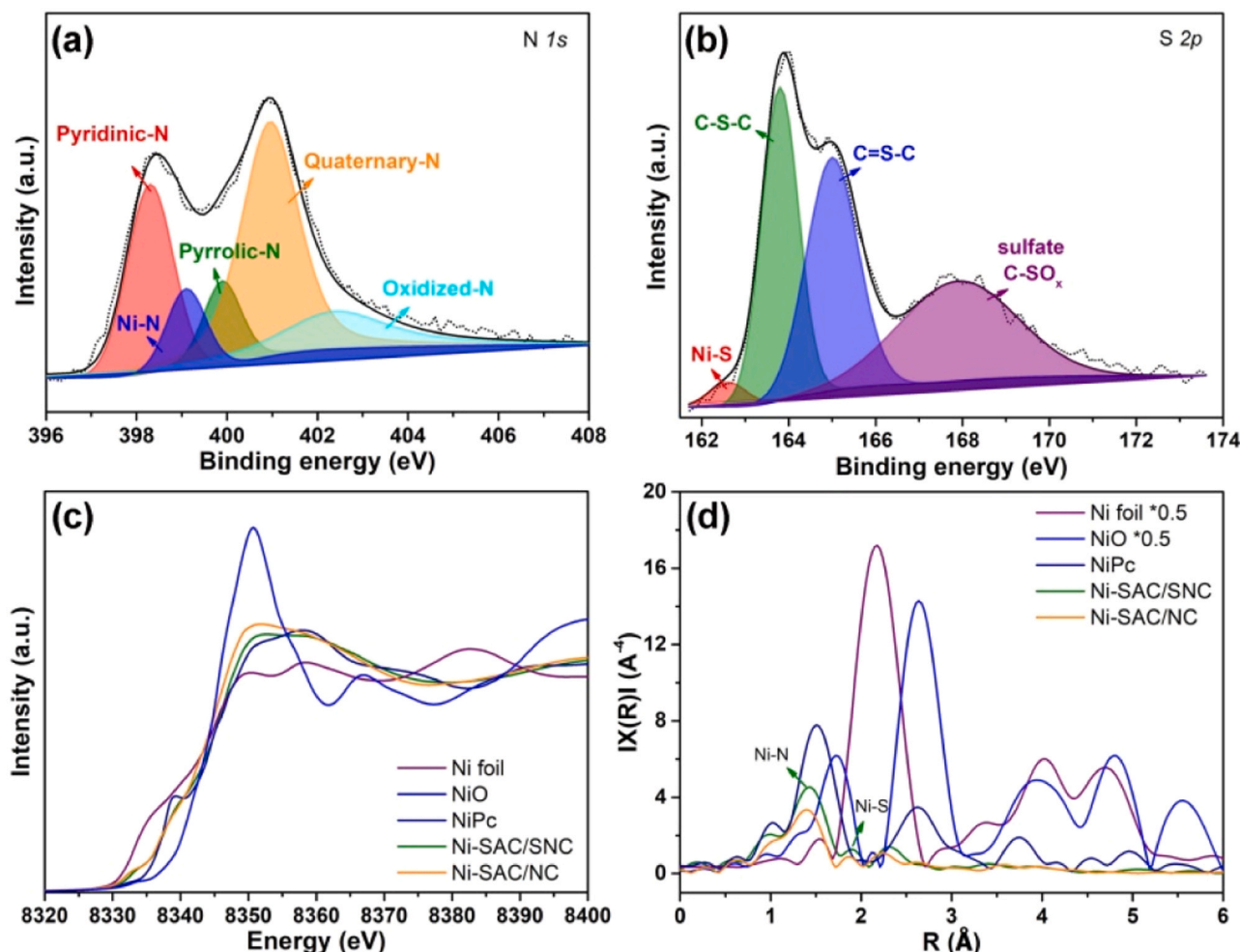


Fig. 3. Chemical state and atomic coordination environment of Ni-SAC/SNC. (a) $N1s$ and (b) $S2p$ XPS of Ni-SAC/SNC; (c) Ni K -edge XANES and (d) k^3 -weighted EXAFS of Ni-SAC/SNC and Ni-SAC/NC.

CO_2RR performance, the morphology of Ni-SAC/SNC remained stable without any visible Ni nanoparticles (Fig. S16).

Tafel analysis was further conducted to identify the kinetic mechanism of these catalysts (Fig. 4d) [62]. Ni-SAC/SNC and Ni-SAC/NC displayed a Tafel slope of 124.1 and 156.1 $mV\ dec^{-1}$, respectively. Obviously, the first electron transfer for CO_2 activation is the rate-determining step (RDS) during CO_2RR for both catalysts [63]. The smaller value of Ni-SAC/SNC suggested fast initial electron transfer to CO_2 for CO_2 activation, in agreement with the DFT studies [64]. The fast electron transfer was also supported by a lower interfacial charge transfer resistance (R_{ct}) of Ni-SAC/SNC (52.9 Ω) than Ni-SAC/NC (62.4 Ω) (Fig. S17). Hence, the unique Ni-S configuration largely improved the stability of $COOH^*$ on Ni-SAC/SNC, and directly expedited CO production during CO_2RR . Moreover, since Ni-SAC/SNC and Ni-SAC/NC exhibited a similar electrochemical active surface area (ECSA), a comparable number of active sites in two catalysts was also realized (Fig. S18, S19 and Table S4). Considering the activity difference in CO_2RR between these two catalysts, it was concluded that the unique Ni-S bonding in Ni-N₃S₁ enhanced the electronic localization of Ni with a promoted intrinsic activity by combining the theoretical and experimental measurements.

4. Conclusions

In summary, we have presented a theory-guided design of sulfur-doped single Ni atom catalyst with the optimized Ni-S dual active

moiety supported on hollow nitrogen doped carbon sphere for efficient CO_2RR . Experiments combined with theory verified that Ni-S bonding immensely reduced the electron-deficient state of Ni compared to the S-free counterpart. Such enhanced electronic localization stabilized the key $COOH^*$ intermediate on Ni, and hence boosted CO production. The as-synthesized Ni-SAC/SNC showed a high FE_{CO} ($\sim 98\%$), j_{CO} ($\sim 32.5\ mA\ cm^{-2}$), TOF ($\sim 5860\ h^{-1}$) and remarkable durability ($\sim 24\ h$) at a low overpotential of 620 mV, surpassing most of the reported single-atom electrocatalysts. These findings present the scientific comprehension of the relevance between the electronic density of atomic sites and CO_2RR performance, and show the potential of the theory-guided rational design of catalysts.

CRediT authorship contribution statement

X.S. performed the experiments, collected and analyzed the data, and wrote the paper. L.W., C.Y. and Q.L. helped with data analysis and discussions. X.L. and C.X. helped with discussions. Y.T. performed DFT calculations. D.W. conceived the experiments and wrote the paper.

Declaration of Competing Interest

The authors declare that they have no known competing financial interests or personal relationships that could have appeared to influence the work reported in this paper.

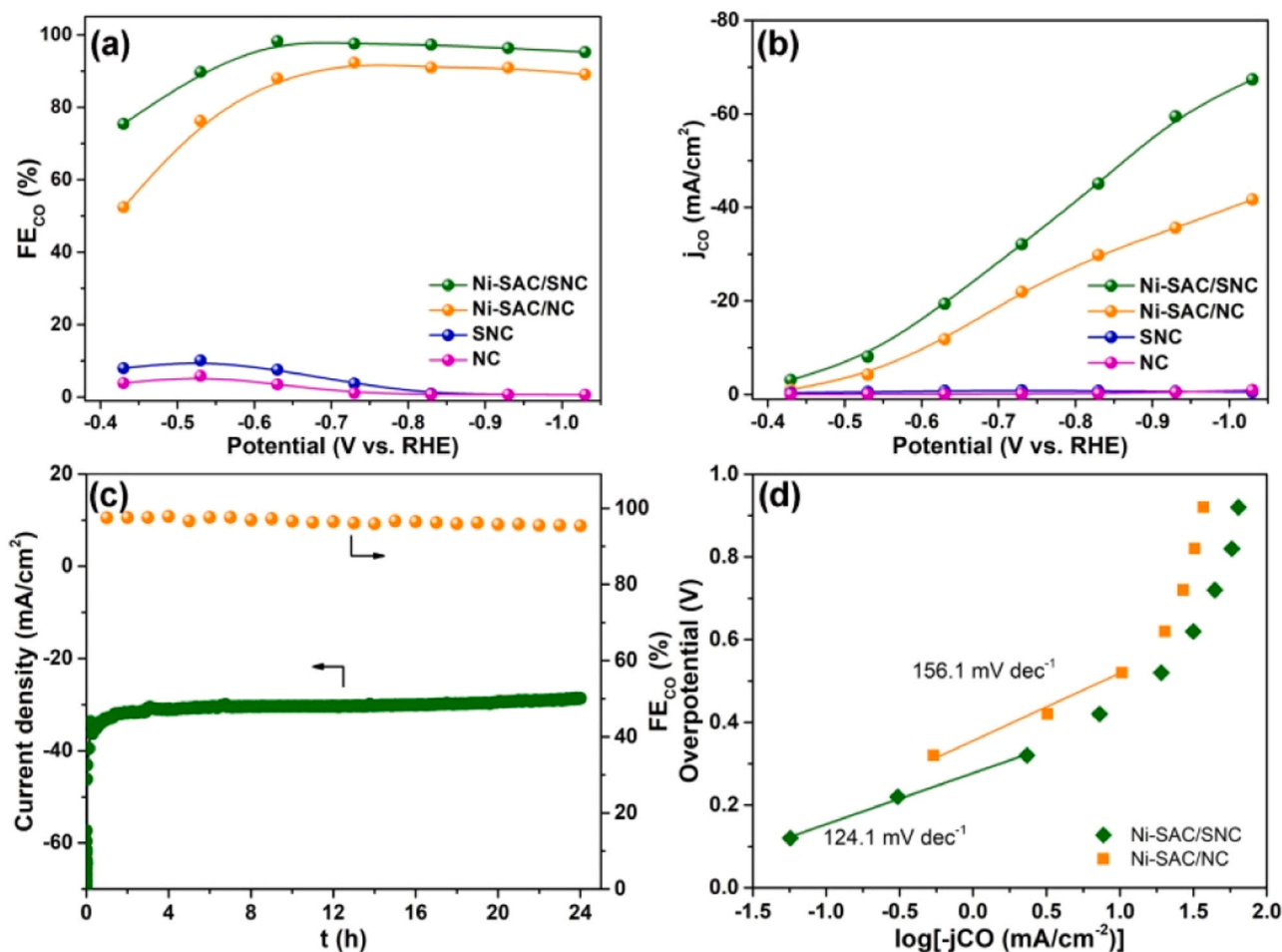


Fig. 4. CO₂RR performance of Ni-SAC/SNC. (a) FE_{CO} and (b) j_{CO} of Ni-SAC/SNC, Ni-SAC/NC, SNC and NC; (c) stability test of Ni-SAC/SNC at -0.73 V vs. RHE; (d) Tafel slope of Ni-SAC/SNC and Ni-SAC/NC.

Data Availability

Data will be made available on request.

Acknowledgments

This work was supported by National Natural Science Foundation of China (22102080), and Science Foundation of China University of Petroleum (Beijing) (ZX20230067). The authors thank the BL14W1 station in Shanghai Synchrotron Radiation Facility (SSRF) and the 1W1B station in Beijing Synchrotron Radiation Facility (BSRF) for XAFS test.

Appendix A. Supporting information

Supplementary data associated with this article can be found in the online version at [doi:10.1016/j.apcatb.2023.123389](https://doi.org/10.1016/j.apcatb.2023.123389).

References

- [1] D. Gao, R.M. Arán-Ais, H.S. Jeon, B. Roldan Cuenya, Rational catalyst and electrolyte design for CO₂ electroreduction towards multicarbon products, *Nat. Catal.* 2 (2019) 198–210.
- [2] D. Gao, Y. Zhang, Z. Zhou, F. Cai, X. Zhao, W. Huang, Y. Li, J. Zhu, P. Liu, F. Yang, G. Wang, X. Bao, Enhancing CO₂ electroreduction with the metal–oxide interface, *J. Am. Chem. Soc.* 139 (2017) 5652–5655.
- [3] X. Feng, K. Jiang, S. Fan, M.W. Kanan, Grain-boundary-dependent CO₂ electroreduction activity, *J. Am. Chem. Soc.* 137 (2015) 4606–4609.
- [4] S. Back, H. Kim, Y. Jung, Selective heterogeneous CO₂ electroreduction to methanol, *ACS Catal.* 5 (2015) 965–971.
- [5] X. Sun, A.I.O. Suarez, M. Meijerink, T. van Deelen, S. Ould-Chikh, J. Zečević, K. P. de Jong, F. Kapteijn, J. Gascon, Manufacture of highly loaded silica-supported cobalt Fischer–Tropsch catalysts from a metal organic framework, *Nat. Commun.* 8 (2017) 1680.
- [6] D. Degerman, M. Shipilin, P. Lömker, C.M. Goodwin, S.M. Gericke, U. Hejral, J. Glad, H.-Y. Wang, C. Schlueter, A. Nilsson, P. Amann, Operando observation of oxygenated intermediates during CO₂ hydrogenation on Rh single crystals, *J. Am. Chem. Soc.* 144 (2022) 7038–7042.
- [7] C. Göbel, S. Schmidt, C. Froese, Q. Fu, Y.-T. Chen, Q. Pan, M. Muhler, Structural evolution of bimetallic Co–Cu catalysts in CO₂ hydrogenation to higher alcohols at high pressure, *J. Catal.* 383 (2020) 33–41.
- [8] Y. Zang, T. Liu, P. Wei, H. Li, Q. Wang, G. Wang, X. Bao, Selective CO₂ electroreduction to ethanol over a carbon-coated CuO_x catalyst, *Angew. Chem. Int. Ed.* 61 (2022), e202209629.
- [9] L. Xu, X. Ma, L. Wu, X. Tan, X. Song, Q. Zhu, C. Chen, Q. Qian, Z. Liu, X. Sun, S. Liu, B. Han, In Situ periodic regeneration of catalyst during CO₂ electroreduction to C₂₊ products, *Angew. Chem. Int. Ed.* 61 (2022), e202210375.
- [10] G. Marcandalli, M.C.O. Monteiro, A. Goyal, M.T.M. Koper, Electrolyte effects on CO₂ electrochemical reduction to CO, *Acc. Chem. Res.* 55 (2022) 1900–1911.
- [11] S. Sharifi Golru, A.S. May, E.J. Biddinger, Modifying copper local environment with electrolyte additives to alter CO₂ electroreduction vs hydrogen evolution, *ACS Catal.* 13 (2023) 7831–7843.
- [12] S. Li, X. Dong, Y. Zhao, J. Mao, W. Chen, A. Chen, Y. Song, G. Li, Z. Jiang, W. Wei, Y. Sun, Chloride ion adsorption enables ampere-level CO₂ electroreduction over silver hollow fiber, *Angew. Chem. Int. Ed.* 61 (2022), e202210432.
- [13] P.-C. Chen, C. Chen, Y. Yang, A.L. Maulana, J. Jin, J. Feijoo, P. Yang, Chemical and structural evolution of AgCu catalysts in electrochemical CO₂ reduction, *J. Am. Chem. Soc.* 145 (2023) 10116–10125.
- [14] H. Wang, Y. Fu, Z.-N. Chen, W. Zhuang, M. Cao, R. Cao, Tunable CO₂ enrichment on functionalized Au surface for enhanced CO₂ electroreduction, *Nano Res.* 16 (2023) 4723–4728.
- [15] S. Liu, C. Sun, J. Xiao, J.-L. Luo, Unraveling structure sensitivity in CO₂ electroreduction to near-unity CO on silver nanocubes, *ACS Catal.* 10 (2020) 3158–3163.

- [16] M.C.O. Monteiro, M.F. Philips, K.J.P. Schouten, M.T.M. Koper, Efficiency and selectivity of CO₂ reduction to CO on gold gas diffusion electrodes in acidic media, *Nat. Commun.* 12 (2021) 4943.
- [17] H. Seong, M. Choi, S. Park, H.-w. Kim, J. Kim, W. Kim, J.S. Yoo, D. Lee, Promoting CO₂-to-CO electroreduction via the active-site engineering of atomically precise silver nanoclusters, *ACS Energy Lett.* 7 (2022) 4177–4184.
- [18] W. Wang, S. Gong, R. Lu, H. Wang, J. Liu, X. Zhu, B. Liu, X. Lv, In situ growth of Ag aerogels mediating effective electrocatalytic CO₂ reduction and Zn-CO₂ batteries, *Chem. Eng. Sci.* 280 (2023), 119042.
- [19] A. Xu, N. Govindarajan, G. Kastlunger, S. Vijay, K. Chan, Theories for electrolyte effects in CO₂ electroreduction, *Acc. Chem. Res.* 55 (2022) 495–503.
- [20] J. Li, A. Zitolo, F.A. Garcés-Pineda, T. Asset, M. Kodali, P. Tang, J. Arbiol, J. R. Galán-Mascarós, P. Atanassov, I.V. Zenyuk, M.T. Sougrati, F. Jaouen, Metal oxide clusters on nitrogen-doped carbon are highly selective for CO₂ electroreduction to CO, *ACS Catal.* 11 (2021) 10028–10042.
- [21] M. Fan, S. Prabhudev, S. Garbarino, J. Qiao, G.A. Botton, D.A. Harrington, A. C. Tavares, D. Guay, Uncovering the nature of electroactive sites in nano architected dendritic Bi for highly efficient CO₂ electroreduction to formate, *Appl. Catal. B Environ.* 274 (2020), 119031.
- [22] S. Vijay, W. Ju, S. Brückner, S.-C. Tsang, P. Strasser, K. Chan, Unified mechanistic understanding of CO₂ reduction to CO on transition metal and single atom catalysts, *Nat. Catal.* 4 (2021) 1024–1031.
- [23] Y. Wang, X. Zheng, D. Wang, Design concept for electrocatalysts, *Nano Res.* 15 (2022) 1730–1752.
- [24] E.R. Cave, C. Shi, K.P. Kuhl, T. Hatsukade, D.N. Abram, C. Hahn, K. Chan, T. F. Jaramillo, Trends in the catalytic activity of hydrogen evolution during CO₂ electroreduction on transition metals, *ACS Catal.* 8 (2018) 3035–3040.
- [25] D. Chen, Z. Pu, P. Wang, R. Lu, W. Zeng, D. Wu, Y. Yao, J. Zhu, J. Yu, P. Ji, S. Mu, Mapping hydrogen evolution activity trends of intermetallic Pt-group silicides, *ACS Catal.* 12 (2022) 2623–2631.
- [26] J.-d. Yi, X. Gao, H. Zhou, W. Chen, Y. Wu, Design of Co-Cu diatomic site catalysts for high-efficiency synergistic CO₂ electroreduction at industrial-level current density, *Angew. Chem. Int. Ed.* 61 (2022), e202212329.
- [27] Y. Li, X.F. Lu, S. Xi, D. Luan, X. Wang, X.W. Lou, Synthesis of N-doped highly graphitic carbon urchin-like hollow structures loaded with single-Ni atoms towards efficient CO₂ electroreduction, *Angew. Chem. Int. Ed.* 61 (2022), e202201491.
- [28] C.D. Koolen, W. Luo, A. Züttel, From single crystal to single atom catalysts: structural factors influencing the performance of metal catalysts for CO₂ electroreduction, *ACS Catal.* 13 (2023) 948–973.
- [29] Y. Zhang, K. Qi, J. Li, B.A. Karamoko, L. Lajounie, F. Godiard, E. Oliviero, X. Cui, Y. Wang, Y. Zhang, H. Wu, W. Wang, D. Voiry, 2.6% cm⁻² single-pass CO₂-to-CO conversion using Ni single atoms supported on ultra-thin carbon nanosheets in a flow electrolyzer, *ACS Catal.* 11 (2021) 12701–12711.
- [30] M.D. Hossain, Y. Huang, T.H. Yu, W.A. Goddard III, Z. Luo, Reaction mechanism and kinetics for CO₂ reduction on nickel single atom catalysts from quantum mechanics, *Nat. Commun.* 11 (2020) 2256.
- [31] C. Wang, X. Hu, X. Hu, X. Liu, Q. Guan, R. Hao, Y. Liu, W. Li, Typical transition metal single-atom catalysts with a metal-pyridine N structure for efficient CO₂ electroreduction, *Appl. Catal. B: Environ.* 296 (2021), 120331.
- [32] K. Wang, B. Chen, Y. Xuan, W. Fan, N. Sun, S. Chang, G. Meng, Efficient utilization of nickel single atoms for CO₂ electroreduction by constructing 3D interconnected nitrogen-doped carbon tube network, *Appl. Catal. B: Environ.* 338 (2023), 123083.
- [33] X.-M. Liang, H.-J. Wang, C. Zhang, D.-C. Zhong, T.-B. Lu, Controlled synthesis of a Ni₂ dual-atom catalyst for synergistic CO₂ electroreduction, *Appl. Catal. B: Environ.* 322 (2023), 122073.
- [34] N. Mohd Adli, W. Shan, S. Hwang, W. Samarakoon, S. Karakalos, Y. Li, D.A. Cullen, D. Su, Z. Feng, G. Wang, G. Wu, Engineering atomically dispersed FeN₄ active sites for CO₂ electroreduction, *Angew. Chem. Int. Ed.* 60 (2021) 1022–1032.
- [35] H.B. Yang, S.-F. Hung, S. Liu, K. Yuan, S. Miao, L. Zhang, X. Huang, H.-Y. Wang, W. Cai, R. Chen, J. Gao, X. Yang, W. Chen, Y. Huang, H.M. Chen, C.M. Li, T. Zhang, B. Liu, Atomically dispersed Ni(I) as the active site for electrochemical CO₂ reduction, *Nat. Energy* 3 (2018) 140–147.
- [36] X. Rong, H.-J. Wang, X.-L. Lu, R. Si, T.-B. Lu, Controlled synthesis of a vacancy-defect single-atom catalyst for boosting CO₂ electroreduction, *Angew. Chem. Int. Ed.* 59 (2020) 1961–1965.
- [37] R.G. Mariano, M. Kang, O.J. Wahab, I.J. McPherson, J.A. Rabinowitz, P.R. Unwin, M.W. Kanan, Microstructural origin of locally enhanced CO₂ electroreduction activity on gold, *Nat. Mater.* 20 (2021) 1000–1006.
- [38] J. Bok, S.Y. Lee, B.-H. Lee, C. Kim, D.L.T. Nguyen, J.W. Kim, E. Jung, C.W. Lee, Y. Jung, H.S. Lee, J. Kim, K. Lee, W. Ko, Y.S. Kim, S.-P. Cho, J.S. Yoo, T. Hyeon, Y. J. Hwang, Designing atomically dispersed Au on tensile-strained Pd for efficient CO₂ electroreduction to formate, *J. Am. Chem. Soc.* 143 (2021) 5386–5395.
- [39] S. Gong, W. Wang, R. Lu, M. Zhu, H. Wang, Y. Zhang, J. Xie, C. Wu, J. Liu, M. Li, S. Shao, G. Zhu, X. Lv, Mediating heterogenized nickel phthalocyanine into isolated Ni-N₃ moiety for improving activity and stability of electrocatalytic CO₂ reduction, *Appl. Catal. B: Environ.* 318 (2022), 121813.
- [40] J. Zhang, H. Yang, B. Liu, Coordination engineering of single-atom catalysts for the oxygen reduction reaction: a review, *Adv. Energy Mater.* 11 (2021) 2002473.
- [41] J. Zhang, Y. Zhao, C. Chen, Y.-C. Huang, C.-L. Dong, C.-J. Chen, R.-S. Liu, C. Wang, K. Yan, Y. Li, G. Wang, Tuning the coordination environment in single-atom catalysts to achieve highly efficient oxygen reduction reactions, *J. Am. Chem. Soc.* 141 (2019) 20118–20126.
- [42] X. Li, H. Rong, J. Zhang, D. Wang, Y. Li, Modulating the local coordination environment of single-atom catalysts for enhanced catalytic performance, *Nano Res.* 13 (2020) 1842–1855.
- [43] Z. Chen, H. Niu, J. Ding, H. Liu, P.-H. Chen, Y.-H. Lu, Y.-R. Lu, W. Zuo, L. Han, Y. Guo, S.-F. Hung, Y. Zhai, Unraveling the origin of sulfur-doped Fe-N-C single-atom catalyst for enhanced oxygen reduction activity: effect of iron spin-state tuning, *Angew. Chem. Int. Ed.* 60 (2021) 25404–25410.
- [44] X. Sun, L. Sun, G. Li, Y. Tuo, C. Ye, J. Yang, J. Low, X. Yu, J.H. Bitter, Y. Lei, D. Wang, Y. Li, Phosphorus tailors the d-band center of copper atomic sites for efficient CO₂ photoreduction under visible-light irradiation, *Angew. Chem. Int. Ed.* 61 (2022), e202207677.
- [45] L. Li, W. Yu, W. Gong, H. Wang, C.-L. Chiang, Y. Lin, J. Zhao, L. Zhang, J.-M. Lee, G. Zou, Sulfur-induced electron redistribution of single molybdenum atoms promotes nitrogen electroreduction to ammonia, *Appl. Catal. B Environ.* 321 (2023), 122038.
- [46] X. Sun, Y. Tuo, C. Ye, C. Chen, Q. Lu, G. Li, P. Jiang, S. Chen, P. Zhu, M. Ma, J. Zhang, J.H. Bitter, D. Wang, Y. Li, Phosphorus induced electron localization of single iron sites for boosted CO₂ electroreduction reaction, *Angew. Chem. Int. Ed.* 60 (2021) 23614–23618.
- [47] J.-X. Peng, W. Yang, Z. Jia, L. Jiao, H.-L. Jiang, Axial coordination regulation of MOF-based single-atom Ni catalysts by halogen atoms for enhanced CO₂ electroreduction, *Nano Res.* 15 (2022) 10063–10069.
- [48] N.C. Strandwitz, G.D. Stucky, Hollow microporous cerium oxide spheres templated by colloidal silica, *Chem. Mater.* 21 (2009) 4577–4582.
- [49] X. Wang, Y. Tuo, Y. Zhou, D. Wang, S. Wang, J. Zhang, Ta-doping triggered electronic structural engineering and strain effect in NiFe LDH for enhanced water oxidation, *Chem. Eng. J.* 403 (2021), 126297.
- [50] S. Chen, X. Li, C.-W. Kao, T. Luo, K. Chen, J. Fu, C. Ma, H. Li, M. Li, T.-S. Chan, M. Liu, Unveiling the proton-feeding effect in sulfur-doped Fe-N-C single-atom catalyst for enhanced CO₂ electroreduction, *Angew. Chem. Int. Ed.* 61 (2022), e202206233.
- [51] G.W. Woyessa, J.-a.B. dela Cruz, M. Rameez, C.-H. Hung, Nanocomposite catalyst of graphitic carbon nitride and Cu/Fe mixed metal oxide for electrochemical CO₂ reduction to CO, *Appl. Catal. B: Environ.* 291 (2021), 120052.
- [52] Z. Xiao, L. Zhao, Z. Yu, M. Zhang, S. Li, R. Zhang, M. Ayub, X. Ma, G. Ning, C. Xu, Multilayered graphene endowing superior dispersibility for excellent low temperature performance in lithium-ion capacitor as both anode and cathode, *Chem. Eng. J.* 429 (2022), 132358.
- [53] X. Sun, R. Wang, S. Ould-Chikh, D. Osadchii, G. Li, A. Aguilar, J.-I. Hazemann, F. Kapteijn, J. Gascon, Structure-activity relationships in metal organic framework derived mesoporous nitrogen-doped carbon containing atomically dispersed iron sites for CO₂ electrochemical reduction, *J. Catal.* 378 (2019) 320–330.
- [54] R. Li, D. Wang, Understanding the structure-performance relationship of active sites at atomic scale, *Nano Res.* 15 (2022) 6888–6923.
- [55] X. Zheng, B. Li, Q. Wang, D. Wang, Y. Li, Emerging low-nuclearity supported metal catalysts with atomic level precision for efficient heterogeneous catalysis, *Nano Res.* 15 (2022) 7806–7839.
- [56] X. Sun, A.I. Olivos-Suarez, L. Oar-Arteta, E. Rozhko, D. Osadchii, A. Bavykina, F. Kapteijn, J. Gascon, Metal–Organic Framework Mediated Cobalt/Nitrogen-Doped Carbon Hybrids as Efficient and Chemoselective Catalysts for the Hydrogenation of Nitroarenes, *ChemCatChem* 9 (2017) 1854–1862.
- [57] Z. Xiao, Z. Yu, Z. Gao, B. Li, M. Zhang, C. Xu, S-doped graphene nano-capsules toward excellent low-temperature performance in Li-ion capacitors, *J. Power Sources* 535 (2022), 231404.
- [58] Y. Li, H. Zhang, Y. Wang, P. Liu, H. Yang, X. Yao, D. Wang, Z. Tang, H. Zhao, A self-sponsored doping approach for controllable synthesis of S and N co-doped trimodal-porous structured graphitic carbon electrocatalysts, *Energy Environ. Sci.* 7 (2014) 3720–3726.
- [59] H. Shang, X. Zhou, J. Dong, A. Li, X. Zhao, Q. Liu, Y. Lin, J. Pei, Z. Li, Z. Jiang, D. Zhou, L. Zheng, Y. Wang, J. Zhou, Z. Yang, R. Cao, R. Sarangi, T. Sun, X. Yang, X. Zheng, W. Yan, Z. Zhuang, J. Li, W. Chen, D. Wang, J. Zhang, Y. Li, Engineering unsymmetrically coordinated Cu-S₃N₃ single atom sites with enhanced oxygen reduction activity, *Nat. Commun.* 11 (2020) 3049.
- [60] Y. Hou, M. Qiu, M.G. Kim, P. Liu, G. Nam, T. Zhang, X. Zhuang, B. Yang, J. Cho, M. Chen, C. Yuan, L. Lei, X. Feng, Atomically dispersed nickel-nitrogen-sulfur species anchored on porous carbon nanosheets for efficient water oxidation, *Nat. Commun.* 10 (2019) 1392.
- [61] T. Zhang, Z. Chen, A.G. Walsh, Y. Li, P. Zhang, Single-atom catalysts supported by crystalline porous materials: views from the inside, *Adv. Mater.* 32 (2020) 2002910.
- [62] T. Li, C. Yang, J.-L. Luo, G. Zheng, Electrolyte driven highly selective CO₂ electroreduction at low overpotentials, *ACS Catal.* 9 (2019) 10440–10447.
- [63] J. Zhou, W. Yan, Z. Gan, C. Shu, Z. Zheng, W. Tang, T. Wu, K. Xie, M. Ma, Layer-stacked Zn with abundant corners for selective CO₂ electroreduction to CO, *ACS Appl. Energy Mater.* 6 (2023) 2954–2961.
- [64] S. Li, W. Chen, X. Dong, C. Zhu, A. Chen, Y. Song, G. Li, W. Wei, Y. Sun, Hierarchical micro/nanostructured silver hollow fiber boosts electroreduction of carbon dioxide, *Nat. Commun.* 13 (2022) 3080.